DOI: 10.1002/((please add manuscript number))
Article type: Communication

Efficient and Stable Perovskite Solar Cells using Low-cost Aniline-based Enamine Hole Transporting Materials

Deimante Vaitukaityte, Zhiping Wang, Tadas Malinauskas, Artiom Magomedov, Giedre Bubniene, Vygintas Jankauskas, Vytautas Getautis* and Henry J. Snaith**

D. Vaitukaityte, Dr. T. Malinauskas, A. Magomedov, Dr. G. Bubniene, Prof. V. Getautis
Department of Organic Chemistry, Kaunas University of Technology, Radvilenu pl. 19, Kaunas, 50254, Lithuania
E-mail: vytautas.getautis@ktu.lt
Dr. Z. Wang, Prof. H. J. Snaith
Clarendon Laboratory, Department of Physics, University of Oxford, Parks Road, Oxford, OX1 3PU, United Kingdom
E-mail: zhiping.wang@physics.ox.ac.uk; henry.snaith@physics.ox.ac.uk
Dr. V. Jankauskas
Department of Solid State Electronics, Vilnius University, Sauletekio 9, Vilnius 10222, Lithuania

Keywords: aldehyde; aniline; enamine; perovskite solar cell; semiconductors

During the past several years perovskite solar cell (PSC) technology has evolved from a scientific curiosity to a major research subject in the field of photovoltaics. In that short period of time they have gained recognition as one of the most promising photovoltaic technologies and managed to demonstrate remarkable achievements in the power conversion efficiency (PCE) exceeding 22%[1] and rivalling other thin-film technologies as well as silicon photovoltaic devices.[2] The remarkable device performances can be attributed to excellent optoelectronic properties of metal halide perovskites, such as low exciton binding energy,[3] high charge carrier mobility,[4,5] high absorption coefficient[6,7] and long carrier diffusion

length.[8,9] To date, most of the high efficiency negative(n)-intrinsic(i)-positive(p) structured perovskite solar cells are based on either 2,2′,7,7′-tetrakis(*N*,*N*-di-*p*-methoxy-phenylamine)-9-9′-spirobifluorene (spiro-OMeTAD) or poly[bis(4-phenyl)(2,4,6-trimethylphenyl)amine] (PTAA) hole-transporting materials (HTMs), both of which are very expensive.[10-12] The generated high cost is mainly due to the following reasons: (i) multi-step synthesis; (ii) complicated purification procedures[13]; (iii) sublimation steps for purification and (iv) use of transition metal catalysts. For step iv, tiny amount of the catalysts, *i.e.*, palladium, would remain in the grained HTMs, which may serve as traps that deteriorating the charge-transporting properties of the synthesized HTMs and result in poor device performance.[14, 15] To remove the catalyst residue, sophisticated purification procedures, such as sublimation or repeated column chromatography, are typically required, which would greatly reduce the material yield and therefore further increase the final costs.

Aniline, as one of the most basic and widely used precursors in chemical industry, has been used in synthesis of numerous chemicals and is extremely cheap and produced on a vast scale (over 7 million tons/year).[16] Use of such a low cost and readily available reagent as a starting material could be beneficial from both practical and commercial points of view.

Herein, we synthesize enamine-based HTMs using aniline precursors and further adopt a cost-effective single step, transition-metal-catalysts-free route which we established previously.[17] We demonstrate that perovskite solar cells with the synthesized HTMs exhibit comparable high efficiencies and greatly enhanced ambient-air stability in contrast to the cells with the state-of-art spiro-OMeTAD HTM.

We synthesize the HTMs by reacting the aniline precursor with 2,2-bis(4-methoxyphenyl)acetaldehyde in the presence of (+/-)camphor sulfonic acid (CSA). Depending on the ration of the reagents, enamines with two (**V1092**) or three (**V1091**) diphenylethenyl groups have been isolated (Scheme 1a). Additionally, aniline derivatives with a methoxy group in *para*-position (**V1056**) and 3,5-dimethyl substituted analogue (**V1102**)

were also used for the synthesis (Scheme 1b). The methoxy group serves as an additional donor and blocks the *para*-position of the phenyl ring. The 3,5-dimethyaniline was chosen due to its beneficial influence on device performance.[18] Different from the synthesis of the conventional HTMs used in PSCs,[19] we do not need any transition metal catalysts during the synthesis of these enamines, and the problematic catalysts-residual-induced recombination[20–22] as mentioned above is no longer a major concern. Another advantage of the catalyst-free synthesis is that the purification of the HTMs is largely simplified and oftentimes a basic crystallization is sufficient. Detailed synthesis procedure and analysis can be found in the Supporting Information (SI).

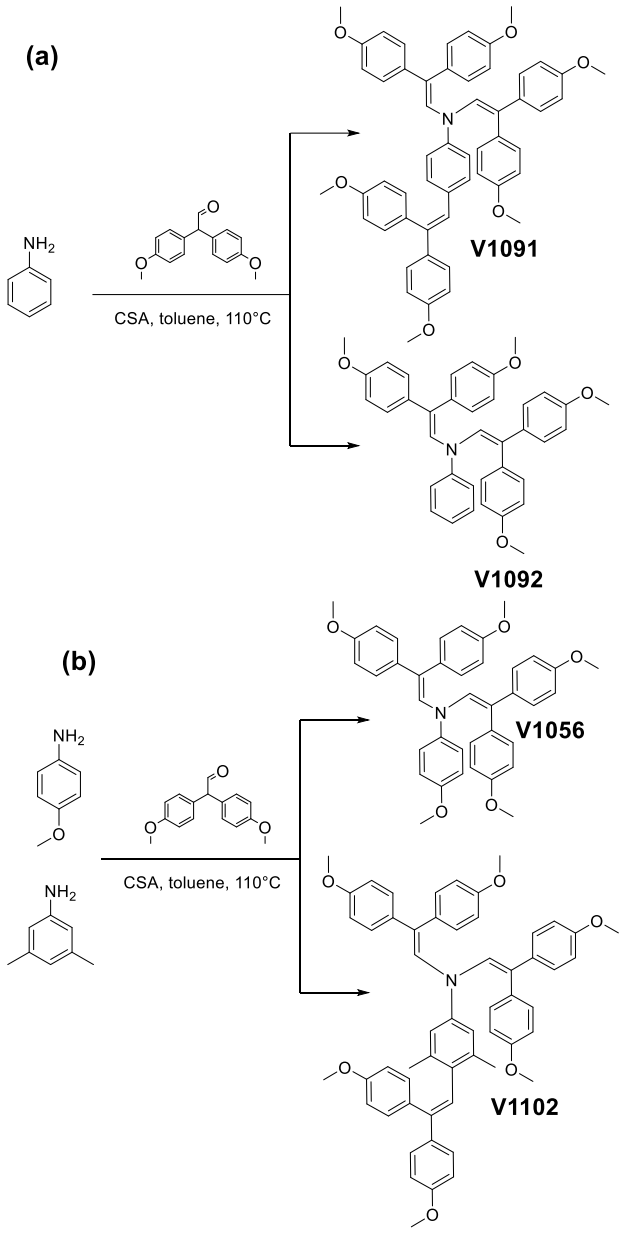

Scheme 1. A single-step synthesis of the HTMs: **V1091**, **V1092** (a); **V1056**, **V1102** (b).

To assess the cost-effectiveness of the HTMs, we performed materials cost estimations for the synthesis of **V1056** and **V1091** based on the procedure established by Osedach et al. (Table S1 and S2).[23] We estimate the material cost is ~16 \$ g^{-1} for **V1091** and ~8 \$ g^{-1} for **V1056** which are less than 1/5 of the cost of the reference spiro-OMeTAD (~92 \$ g^{-1}).[24]

To examine the thermal stability of the target materials, we applied thermogravimetric (TGA) measurement as we show the data in Figure 1, and give full characteristics in Table 1. We find that all the HTM molecules exhibit excellent thermal stability. Interestingly, we observe a rapid weight loss during TGA experiments, which indicates that the HTMs undergo

sublimation rather than thermal decomposition. This suggests that the HTMs could also be processed by vacuum process which would further widen its applications.

Differential scanning calorimetry (DSC) analysis demonstrated that the relatively smaller molecules with two diphenylethenyl fragments (**V1056** and **V1092**) have a stronger tendency of crystallization than the larger analogues with three diphenylethenyl fragments (**V1091** and **V1102**). Aniline derivative **V1092** shows a relatively high melting temperature (T_m) of 251 °C (Figure 1b); during the second heating glass transition (T_g) is observed at 80 °C followed by recrystallization at 129 °C. The additional methoxy functional group in **V1056** introduces a certain degree of disorder into the molecule and lowers the melting temperature considerably to 190 °C. It also contributes to the stability of the amorphous state; the material no longer crystallizes during second heating and only T_g at 78 °C is observed (Figure 1c). The third diphenylethenyl moiety in *para*-position of the phenyl ring in **V1091** even further hampers crystallization and molecule becomes fully amorphous, it also adds some additional structural bulk, increasing T_g to 109 °C (Figure 1d). Similar picture is observed for **V1102** (Figure 1e), although, glass transition temperature is lower, most likely methyl groups at 3,5-positions of the phenyl ring contribute to the sterical hindrance of the molecule.

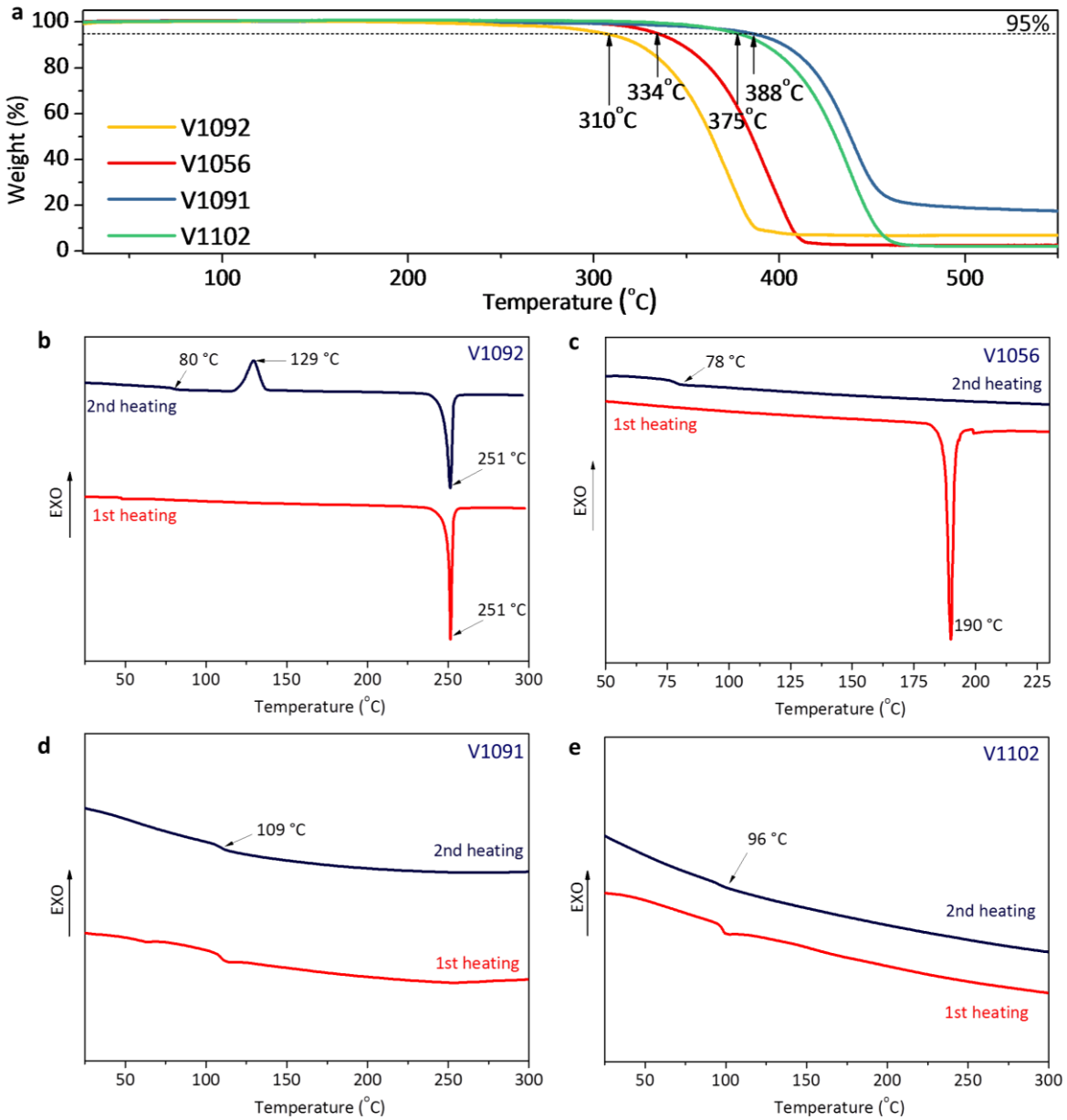

Figure 1. (a) TGA heating curve of **V1092**, **V1056**, **V1091 and V1102** (heating rate 10 K min^{-1}). DSC heating curves of **V1092** (b), **V1056** (c), **V1091** (d) and **V1102** (e) (heating and cooling rate 10 K min^{-1}).

The ultraviolet-visible (UV-vis) absorption spectra of the aniline-based enamines containing two diphenylethenyl groups (**V1056**, **V1092**) showed a bathochromic shift (~ 50 nm) compared with the unsubstituted aniline (Figure 2a). The methoxy group in **V1056** has a negligible effect on the size of the π-conjugated system. A third diphenylethenyl group in

V1091, however, noticeably increases its size, resulting in a ~50 nm bathochromic shift. This confirms that the amine condensation with 2,2-bis(4-methoxy-phenyl)acetaldehyde offers a simple route towards enlarged conjugated system. In fact, the sizes of the π-conjugated system of the spiro-OMeTAD and tri-substituted aniline **V1091** are similar. With the addition of the methyl groups in 3,5-positions of the phenyl ring, **V1102** shows significant changes in the overall size of the π-conjugated system as compared with **V1091**, resulting a hypsochromic shift of ~14 nm. It is likely that the steric hindrance at 4-position of the phenyl ring is increased by the presence of the methyl groups at 3,5-positions. As a consequence, diphenylethenyl moiety becomes more twisted out of the plane.

Table 1. Thermal properties of synthesized HTMs and spiro-OMeTAD**.**

HTM	T_m [ºC]	T_{recr} [ºC]	T_g [ºC][a)]	T_{dec} [ºC]
V1056	190	–	78	334
V1091	–	–	109	388
V1092	251	129	80	310
V1102	–	–	96	375
spiro-OMeTAD	245	–	126	449

[a)] Determined by DSC: scan rate, 10 K min^{-1}; N_2 atmosphere; second run.

Photoelectron spectroscopy in air (PESA) method was used to measure ionization potentials (I_p) of the investigated HTMs (Figure S1, Table 2). Aniline derivative containing two diphenylethenyl groups (**V1092**) exhibits the highest I_p value among all HTMs investigated in this work. Additional electron donating dipheneylethenyl (**V1091**) or methoxy (**V1056**) group lowers the I_p values of the HTMs by ~0.1 eV. With the addition of methyl groups at 3,5-positions of the phenyl ring in **V1102**, we do not see an obvious change in I_p. On the whole, the I_p values of the synthesized HTMs are slightly higher than spiro-OMeTAD, but still suitable for hole extraction in perovskite solar cells.[2]

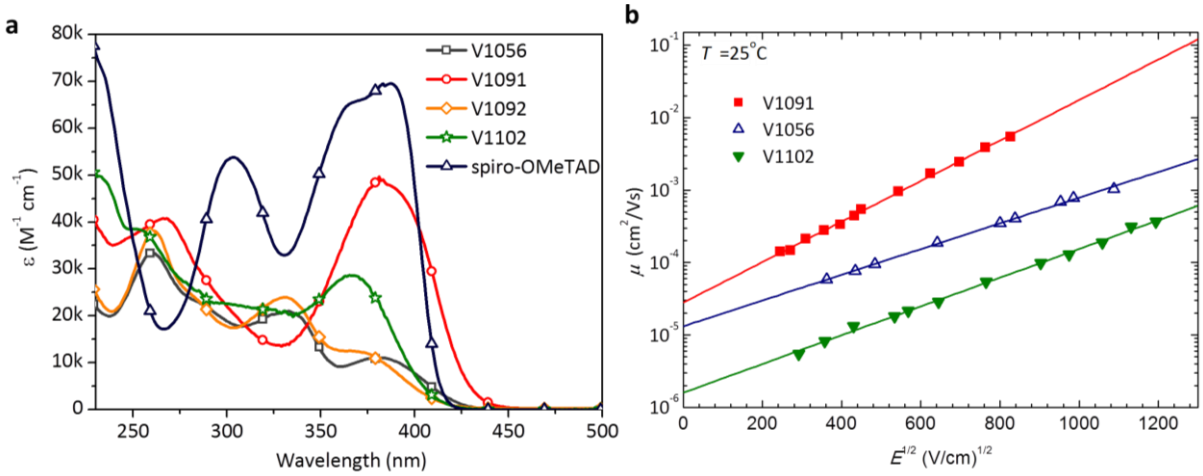

Figure 2. (a) UV–vis absorption spectra of **V1056**, **V1091**, **V1092**, **V1102** and spiro-OMeTAD in THF (c = 10^{-4} M). (b) Electric-field dependencies of the hole drift mobilities in films of **V1056**, **V1091**, and **V1102**.

Table 2. UV-vis absorbance, I_p and hole mobility investigated HTMs and spiro-OMeTAD.

ID	λ_{max}^{abs} [nm]	I_p [eV]	μ_0, [cm^2 V^{-1} s^{-1}] [a)]	μ, [cm^2 V^{-1} s^{-1}] [b)]	α, [cm$^{1/2}$V$^{-1/2}$]
V1056	333, 384	5.19	1.3×10^{-5}	7.8×10^{-4}	0.0041
V1091	381	5.17	2.8×10^{-5}	1.7×10^{-2}	0.0046
V1092	331, 370	5.30	–	–	–
V1102	367	5.16	1.6×10^{-6}	1.5×10^{-4}	0.0064
spiro-OMeTAD	387	5.00	4.1×10^{-5}	5.0×10^{-4}	0.0031

[a)] Mobility value at zero field strength; [b)] Mobility value at 6.4×10^5 V cm^{-1} field strength; [c)] Poole–Frenkel parameter (α).

Charge transport properties of the investigated HTMs were measured using xerographic time-of-flight (XTOF) technique (Figure 2b) and we show the results in Table 2. **V1056**, with the methoxy group at para-position of a phenyl ring, shows a similar hole mobility as compared to spiro-OMeTAD. In contrast, **V1091**, containing three diphenylethenyl moieties, displays significantly better hole drift mobilities at high electric fields. The presence of the methyl groups at 3,5-positions of the phenyl ring in **V1102** results in reduced charge mobility.

To study influence of the methyl groups on the geometry of the **V1102**, molecular geometries of **V1091** and **V1102** were optimized *via* density functional theory (DFT)

calculations with B3LYP/def2-SVP (vacuum) level of theory. Dihedral angle between phenyl plane of aniline and double bond increased from 24.6° in **V1091** to 58.6° in **V1102** after addition of two methyl groups (Figure 3). Generally, increased 3D structural complexity of organic molecules, *i.e.* decreased planarity, would disturb intermolecular π–π packing and leads to difficulties in intermolecular charge carrier hopping.[25-27] We therefore observed decreased mobility in the **V1102** as compared to **V1091**. This is also in good agreement with the DSC results where we observed a higher glass transition temperature for the **V1091** than the **V1102**. Furthermore, from highest occupied molecular orbital (HOMO) of the corresponding molecules (Figure 3), we see that a lower planarity hinders delocalization of the electrons in **V1102** over double bond and results in a smaller π-conjugated system as compared to the **V1091**. Therefore, we would expect a smaller absorption coefficient for the **V1102** than that for the **V1091**. This is consistent with the UV-vis absorption measurement (Figure 2a).

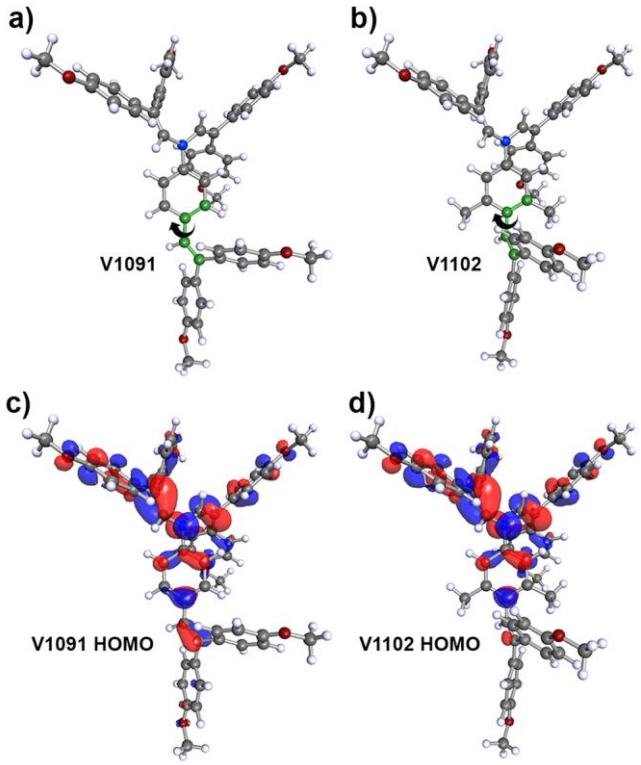

Figure 3. Optimized geometries of the **V1091** (a) and **V1102** (b). HOMO molecular orbitals of the **V1091** (c) and **V1102** (d).

We now proceed to test the synthesized HTMs in planar heterojunction perovskite solar cells (with a device structure: fluorine doped tin oxide (FTO)/SnO_2/perovskite/HTM/Au). A mixed-cation lead mixed-halide $FA_{0.83}Cs_{0.17}Pb(I_{0.9}Br_{0.1})_3$ perovskite was adopted as a photoactive layer.[28, 29] The current density-voltage (*J-V*) characteristics were measured under a simulated AM 1.5G (100 mW cm^{-2}) sunlight and results are presented in Figure 4a and Table 3, while device statistics can be seen in Figure S2. As determined from the forward bias (FB) to short-circuit (SC) current-voltage scan, the device using the **V1102** and **V1056** show a champion efficiency of 17.6% and 18.7%, respectively, which is slightly lower than the PCE of 20.2% for the control device using the spiro-OMeTAD. In contrast, the PSC using **V1091** exhibits a high efficiency of 20.2% with a J_{sc} of 22.5 mA cm^{-2}, a V_{oc} of 1.11 V and a FF of 0.81. The devices containing investigated HTMs showed very similar external quantum efficiency (EQE) spectra to that of the spiro-OMeTAD device (Figure 4b), which is consistent with the similar J_{sc} observed in the *J-V* scans. Due to the hysteretic behavior of perovskite solar cells, a stabilized efficiency measurement was performed to accurately access the performance of the PSC (Figure 4c). By holding the cells at a fixed maximum power point forward bias voltage, we measure the stabilized power output (SPO) over time, achieving a stabilized efficiency of 19.8% for the control device and 18.4% for the **V1091** device. Furthermore, we find that device performance varies significantly with the thickness of the spiro-OMeTAD, as shown in Figure S6 in the Supporting Information. In contrast, the performance of the V1091 devices is less sensitive to the thickness of V1091. We note that when increasing the thickness of the V1091, we need a longer time for oxidization to reach the peak efficiency. Understanding and accelerating the oxidization process is a subject of ongoing study.

On the whole, PSC containing **V1091** and spiro-OMeTAD showed comparable performance.

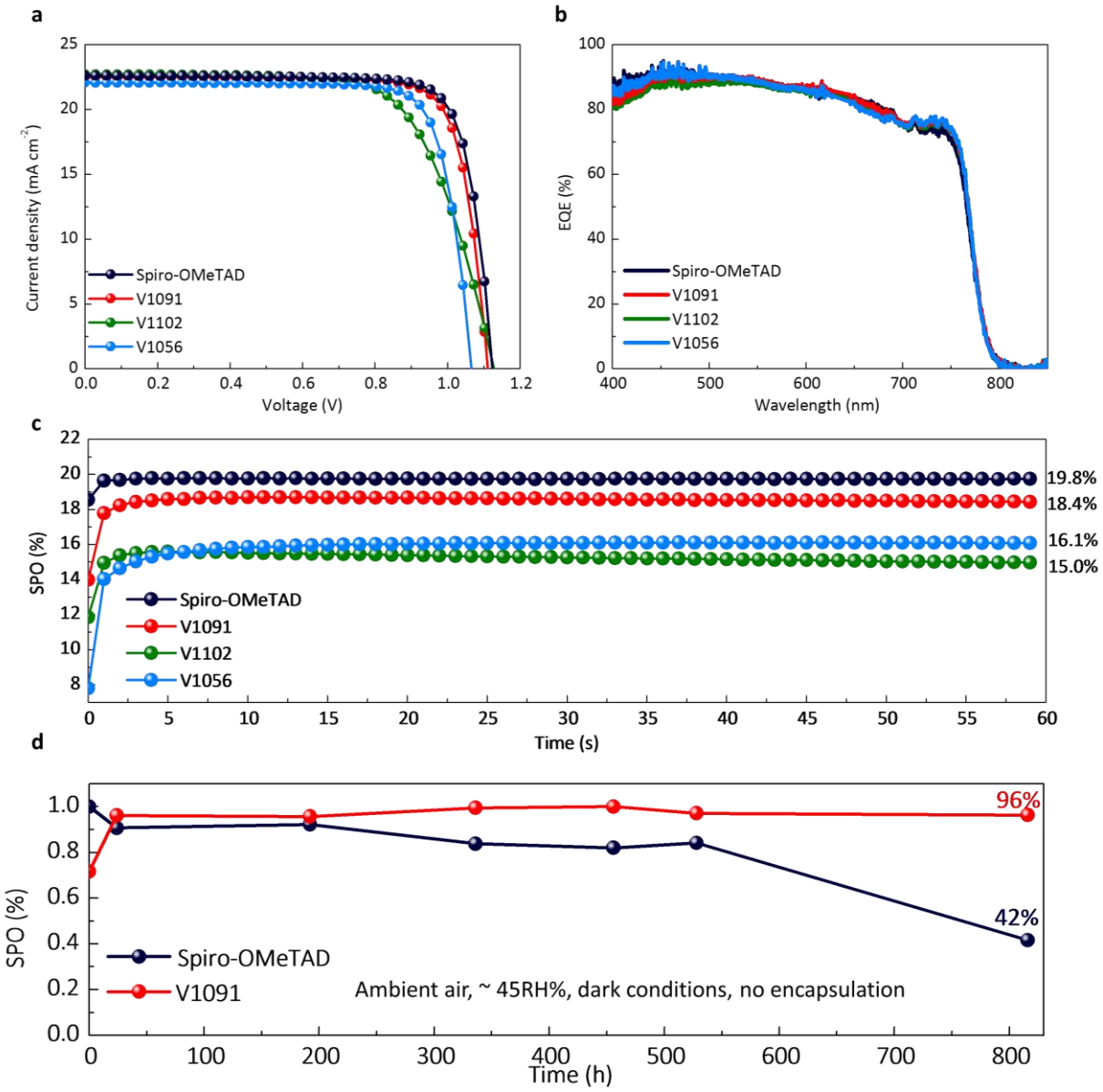

Figure 4. (a) *J-V* characteristics of the best performing PSC devices using V1091, V1102, V1056 and spiro-OMeTAD. (b) Corresponding EQE spectra as a function of the wavelength of monochromatic light. (c) Stabilized power output (SPO) over time of the devices containing investigated HTMs and spiro-OMeTAD. (d) Decay of SPO of devices with spiro-OMeTAD (navy) and **V1091** (red). The device structure is FTO/SnO_2/perovskite/HTM/Au. The devices are in ambient air with a relative humidity of ~ 45% under dark conditions without encapsulation.

To access the device stability using the HTMs, we aged non-encapsulated high efficiency devices with the **V1091** and spiro-OMeTAD hole transporting layers in ambient air with a relative humidity of ~ 45% under dark conditions and measured under an AM 1.5 G solar simulator at different time intervals, the decay of the SPO is shown in Figure 4d. The **V1091** device showed superior stability sustaining 96% of its original efficiency after 820 h. In contrast, the SPO of the control device dropped to 42% after aging. The Li-TFSI was used as a dopant for both the **V1091** and spiro-OMeTAD. Previous studies observed that devices using the Li-TFSI doped spiro-OMeTAD show moisture instability due to the hygroscopic nature of Li-TFSI,[30, 31] which can be the reason for the observed fast decay of efficiency in the control device. Surprisingly, the **V1091** molecule seems to specifically resist this Li-TFSI-induced degradation. To better understand the stability enhancement, we measured the UV-vis absorption spectra of the HTMs in solutions and thin films, as we show the results in Figure S3. Generally, the molecules in solution do not have a particular packing, which is random. For **V1091**, we observe a bathochromic shift of absorption maximum and broadening of the spectrum when comparing the thin films with the solution, which is indicative of aggregate formation in the film.[31-33] In contrast, we do not see noticeable change in the spectra of spiro-OMeTAD solution and thin films, suggesting its random molecular packing in the thin film (Figure S4). Furthermore, we carried out contact angle (θ) measurement to assess the hydrophobicity of the HTMs (Figure S5). We do not see an obvious change in θ between the pristine (undoped) spiro-OMeTAD and **V1091** films. However, we surprisingly discover that with the addition of Li-TFSI and *t*BP dopants, the **V1091** film displays a clearly more hydrophobic surface with a θ of 71.2° than the spiro-OMeTAD film with a θ of 65.4°. Both of the improved molecular packing and a more hydrophobic surface for the V1091 film would retard the ambient moisture ingression, which directly contributed to the improved stability.

Table 3. Summary of solar cell characteristics.

ID		J_{sc} [mA cm^{-2}]	V_{oc} [V]	FF	PCE [%]
spiro-OMeTAD	Average	22.6±0.24	1.11±0.03	0.75±0.03	18.4±1.0
	Champion	22.6	1.12	0.80	20.2
V1091	Average	22.0±0.27	1.11±0.05	0.77±0.03	17.0±2.5
	Champion	22.5	1.11	0.81	20.2
V1102	Average	22.0±0.64	1.05±0.07	0.59±0.06	13.5±2.5
	Champion	22.7	1.13	0.68	17.6
V1056	Average	22.1±0.15	1.03±0.03	0.78±0.05	17.5±1.2
	Champion	22.1	1.07	0.79	18.7

In conclusion, we have developed a new group of aniline-based HTMs obtainable *via* one-step synthetic procedure from low-cost aniline starting materials without use of expensive and problematic oraganometallic catalysts. The material costs have been greatly reduced to less than 1/5 of that for spiro-OMeTAD. Perovskite solar cells using these cheap HTMs show comparable efficiency to the cells using the expensive spiro-OMeTAD HTM. Importantly, perovskite solar cells using enamine **V1091** shows significantly enhanced ambient stability in contrast to the cells using spiro-OMeTAD. The cost-effective, efficient and stable aniline-based enamines offer great opportunities for up-scaling perovskite solar cells. Furthermore, these materials can be processed via both solution and vacuum processes, which we believe would open up possibilities for the interlayers for large-area perovskite-perovskite tandem cells as well as many other opto-electronic device applications.

Supporting Information

Supporting Information is available from the Wiley Online Library or from the author.

Acknowledgements

The research leading to these results has received funding from the European Union's Horizon 2020 research and innovation programme under grant agreement No. 763977 of the PerTPV project. The authors acknowledge funding from Research Council of Lithuania (grant No.

MIP-17-70). D. V. thanks for the support funded by the European Social Fund under the No 09.3.3.-LMT-K-712-03-0038 “Development of Competences of Scientists, other Researchers and Students through Practical Research Activities” measure. Z.W. and H.J.S acknowledge AFOSR through project FA9550-15-1-0115. D.V. and Z.W. contributed equally to this work.

Received: ((will be filled in by the editorial staff))
Revised: ((will be filled in by the editorial staff))
Published online: ((will be filled in by the editorial staff))

References

[1] W. S. Yang, B.-W. Park, E. H. Jung, N. J. Jeon, Y. C. Kim, D. U. Lee, S. S. Shin, J. Seo, E. K. Kim, J. H. Noh, S. I. Seok, *Science* **2017**, *356*, 1376.

[2] J.-P. Correa-Baena, A. Abate, M. Saliba, W. Tress, T. J. Jacobsson, M. Grätzel, A. Hagfeldt, *Energy Environ. Sci*. **2017**, *10*, 710.

[3] S. Park, J. H. Heo, C. H. Cheon, H. Kim, S. H. Im and H. J. Son, *J. Mater. Chem. A* **2015**, *3*, 24215.

[4] O. Malinkiewicz, A. Yella, Y. H. Lee, G. M. Espallargas, M. Graetzel, M. K. Nazeeruddin and H. J. Bolink, *Nat. Photonics*, **2013**, *8*, 128.

[5] S. Kazim, M. K. Nazeeruddin, M. Gratzel and S. Ahmad, *Angew. Chem., Int. Ed*. **2014**, 53, 2812.

[6] H.-S. Kim, C.-R. Lee, J.-H. Im, K.-B. Lee, T. Moehl, A. Marchioro, S.-J. Moon, R. Humphry-Baker, J.-H. Yum, J. E. Moser, M. Gratzel and N.-G. Park, *Sci. Rep.* **2012**, *2*, 591.

[7] N.-G. Park, *J. Phys. Chem. Lett*. **2013**, *4*, 2423.

[8] S. D. Stranks, G. E. Eperon, G. Grancini, C. Menelaou, M. J. P. Alcocer, T. Leijtens, L. M. Herz, A. Petrozza, H. J. Snaith, *Science* **2013**, *342*, 341.

[9] G. Xing, N. Mathews, S. Sun, S. S. Lim, Y. M. Lam, M. Grätzel, S. Mhaisalkar, T. C. Sum, *Science* **2013**, *342*, 344.

[10] H. Tan, A. Jain, O. Voznyy, X. Lan, F. P. García de Arquer, J. Z. Fan, R. Quintero-Bermudez, M. Yuan, B. Zhang, Y. Zhao, F. Fan, P. Li, L. N. Quan, Y. Zhao, Z.-H. Lu, Z. Yang, S. Hoogland, E. H. Sargent *Science* **2017**, *355*, 722.

[11] Z. Yu, L. Sun, *Adv. Energy Mater.* **2015**, *5*, 1500213.

[12] H. Kim, K.-G. Lima, T.-W. Lee, *Energy Environ. Sci*. **2016**, *9*, 12.

[13] T. P. I. Saragi, T. Spehr, A. Siebert, T. Fuhrmann-Lieker, J. Salbeck, *Chem. Rev*. **2007**, *107*, 1011.

[14] A. Krishna, A. C. Grimsdale, *J. Mater. Chem. A* **2017**, *5*, 16446.

[15] M. P. Nikiforov, B. Lai, W. Chen, S. Chen, R. D. Schaller, J. Strzalka, J. Maser, S. B. Darling, *Energy Environ. Sci*. **2013**, *6*, 1513.

[16] D. Yuan, L. Tian, Z. Li, H. Jiang, C. Yan, J. Dong, H. Wu, B. Wang, *Sci. Rep.* **2018**, *8*, 3103.

[17] M. Daskeviciene, S. Paek, Z. Wang, T. Malinauskas, G. Jokubauskaite, K. Rakstys, K. T. Cho, A. Magomedov, V. Jankauskas, S. Ahmad, H. J.Snaith, V. Getautis, M. K. Nazeeruddin, *Nano Energy* **2017**, *32*, 551.

[18] T. Matsui, I. Petrikyte, T. Malinauskas, K. Domanski, M. Daskeviciene, M. Steponaitis, P. Gratia, W. Tress, J.-P. Correa-Baena, A. Abate, A. Hagfeldt, M. Grätzel, M. K. Nazeeruddin, V. Getautis, M. Saliba, *ChemSusChem* **2016**, *9*, 2567.

[19] L. Calió, S. Kazim, M. Grätzel, S. Ahmad, *Angew. Chem. Int. Ed.* **2016**, *55*, 14522.

[20] K. Rakstys, M. Saliba, P. Gao, P. Gratia, E. Kamarauskas, S. Paek, V. Jankauskas M. K. Nazeeruddin, *Angew. Chem. Int. Ed.* **2016**, *55*, 7464.

[21] M. Degbia, M. Ben Manaa, B. Schmaltz, N. Berton, J. Boucle, R. Antony, F. Tran Van, Mater., *Sci. Semicond. Process.* **2016**, *43*, 90.

[22] O. Usluer, M. Cloutet, G. Hadziioannou, *ACS Macro Lett*. **2014**, *3*, 1134.

[23] T. P. Osedach, T. L. Andrew, V. Bulovic, *Energ. Environ. Sci.*, **2013**, *6*, 711.

[24] M. L. Petrus, T. Bein, T. J. Dingemans, P. Docampo, *J. Mater. Chem. A*, **2015**, *3*, 12159.

[25] Z. Wang, Y. Zhou, T. Miyadera, M. Chikamatsu, Y. Yoshida, *ACS Appl. Mater. Interfaces*, **2017**, *9*, 43893.

[26] Z. Wang, T. Miyadera, T. Yamanari, Y. Yoshida, *ACS Appl. Mater. Interfaces*, **2014**, *6*, 6369.

[27] Z. Wang, Y. Uemura, Y. Zhou, T. Miyadera, R. Azumi, Y. Yoshida, M. Chikamatsu, *ACS Appl. Mater. Interfaces*, **2015**, *7*, 10814.

[28] Z. Wang, D. P. McMeekin, N. Sakai, S. van Reenen, K. Wojciechowski, J. B. Patel, M. B. Johnston, H. J. Snaith, *Adv. Mater.* **2017**, *29*, 1604186.

[29] Z. Wang, Q. Lin, F. P. Chmiel, N. Sakai, L. M. Herz, H. J. Snaith, *Nature Energy* **2017**, *2*, 17135.

[30] J.-W. Lee, D.-H. Kim, H.-S. Kim, S.-W. Seo, S. M. Cho, N.-G.Park, *Adv. Energy Mater.* **2015**, *5*, 1501310.

[31] M. Kasha, *Radiat. Res.* **1963**, *20*, 55.

[32] M. Más-Montoya, R. A. J. Janssen, *Adv. Funct. Mater.* **2017**, *27*, 1605779.

[33] Y. Ren, A. M. Hiszpanski, L. Whittaker-Brooks, Y.-L. Loo, *ACS Appl. Mater. Interfaces* **2014**, *6*, 14533.

A new group of aniline-based enamine hole transporting materials is synthesized, characterized and tested in perovskite solar cells, yielding a champion power conversion efficiency over 20%. The investigated materials are obtained via one step synthesis procedure, without the use of transition metal catalyst, from very common and inexpensive precursor–aniline.

Keyword
aldehyde, aniline, enamine, perovskite solar cell, semiconductors

D. Vaitukaityte, Z. Wang*, T. Malinauskas, A. Magomedov, G. Bubniene, V. Jankauskas, V. Getautis* and H. J. Snaith*

Efficient and stable Perovskite Solar Cells using Low-cost Aniline-based Enamine Hole Transporting Materials

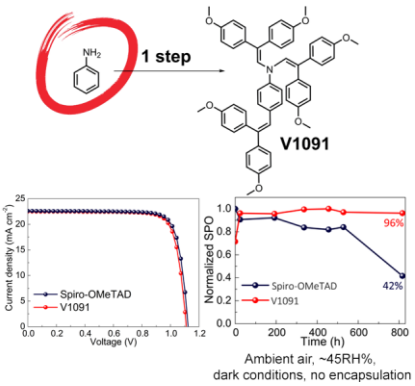

ADVANCED MATERIALS

Supporting Information

Efficient and stable Perovskite Solar Cells using Low-cost Aniline-based Enamine Hole Transporting Materials

Deimante Vaitukaityte, Zhiping Wang, Tadas Malinauskas, Artiom Magomedov, Giedre Bubniene, Vygintas Jankauskas, Vytautas Getautis,* and Henry J. Snaith,**

General methods and materials

Chemicals were purchased from Sigma-Aldrich and TCI Europe and used as received without further purification. The ^{1}H and ^{13}C NMR spectra were taken on Bruker Avance III (400 MHz) spectrometer at RT. All the data are given as chemical shifts in δ (ppm). The course of the reactions products were monitored by TLC on ALUGRAM SIL G/UV254 plates and developed with UV light. Silica gel (grade 9385, 230–400 mesh, 60 Å, Aldrich) was used for column chromatography. Elemental analysis was performed with an Exeter Analytical CE-440 elemental analyser, Model 440 C/H/N/. Differential scanning calorimetry (DSC) was performed on a Q10 calorimeter (TA Instruments) at a scan rate of 10 K min^{-1} in the nitrogen atmosphere. The glass transition temperatures for the investigated compounds were determined during the second heating scan. Electrothermal MEL-TEMP capillary melting point apparatus was used for determination of melting points. UV-vis spectra were recorded on Shimadzu UV-3600 spectrometer.

Ionization Potential Measurements

The solid state ionization potential (I_p) of the layers of the synthesized compounds was measured by the electron photoemission in air method [1, 2]; the measurement error is evaluated as 0.03 eV. The samples for the ionization potential measurement were prepared by dissolving materials in THF and were coated on Al plates pre-coated with ~0.5 μm thick methylmethacrylate and methacrylic acid copolymer adhesive layer. The thickness of the transporting material layer was 0.5-1 μm. Usually photoemission experiments are carried out in vacuum and high vacuum is one of the main requirements for these measurements. If

vacuum is not high enough the sample surface oxidation and gas adsorption are influencing the measurement results. In our case, however, the organic materials investigated are stable enough to oxygen and the measurements may be carried out in the air. The samples were illuminated with monochromatic light from the quartz monochromator with deuterium lamp. The power of the incident light beam was $(2\text{-}5)\cdot10^{-8}$ W. The negative voltage of –300 V was supplied to the sample substrate. The counter-electrode with the 4.5×15 mm^2 slit for illumination was placed at 8 mm distance from the sample surface. The counter-electrode was connected to the input of the BK2-16 type electrometer, working in the open input regime, for the photocurrent measurement. The 10^{-15} – 10^{-12} A strong photocurrent was flowing in the circuit under illumination. The photocurrent I is strongly dependent on the incident light photon energy hν. The $I^{0.5} = f(h\nu)$ dependence was plotted. Usually the dependence of the photocurrent on incident light quanta energy is well described by linear relationship between $I^{0.5}$ and $h\nu$ near the threshold. The linear part of this dependence was extrapolated to the hν axis and I_p value was determined as the photon energy at the interception point.

Hole Drift Mobility Measurements

The samples for the hole mobility measurements were prepared by spin-coating the solutions of the compositions of investigated compounds on polyester films with conductive Al layer. The layer thickness was in the range of 2-6 μm. The hole drift mobility was measured by xerographic time of flight technique (XTOF) [3-5]. Electric field was created by positive corona charging. The charge carriers were generated at the layer surface by illumination with pulses of nitrogen laser (pulse duration was 2 ns, wavelength 337 nm). The layer surface potential decrease as a result of pulse illumination was up to 1-5 % of initial potential before illumination. The capacitance probe that was connected to the wide frequency band electrometer measured the speed of the surface potential decrease dU/dt. The transit time t_t was determined by the kink on the curve of the dU/dt transient in double logarithmic scale. The drift mobility was calculated by the formula $\mu = d^2/U_0 t_t$, where d is the layer thickness, U_0 – the surface potential at the moment of illumination.

Computational details

The theoretical calculations were performed using TURBOMOLE version 7.0 software [6]. Molecular structures of the **V1091** and **V1102** were optimized using Becke's three parameter

functional, B3LYP [7, 8], and def2-SVP [9, 10] basis set in vacuum. Optimized structures and molecular orbitals were visualized with TmoleX version 4.1 software [11].

Photovoltaic device preparation

Electron-transporting layer: 0.05 M $SnCl_4 \cdot 5H_2O$ (Sigma-Aldrich) was first dissolved in anhydrous isopropanol and stirred for 30 min at room temperature. The solution was deposited on cleaned FTO substrates with 3000 rpm spin rate for 30 s, followed by pre-drying at 100 ^oC for 10 min and then heat-treated at 180 ^oC for 1 h. The films were then treated using chemical bath deposition method: 500 mg urea (Sigma-Aldrich) was dissolved in 40 ml deionized water, followed by the addition of 10 ml mercaptopropionic acid (Sigma-Aldrich) and 0.5 ml HCl (37 wt%). Finally, $SnCl_2 \cdot 2H_2O$ (Sigma-Aldrich) was dissolved in the solution at 0.002 M and stirred for 2 min. The deposition was made by putting the substrates in a glass Petri dish filled with the above solution, in a 70 ^oC lab oven for 3 h. The treated substrates were rinsed in a sonication bath of deionized water for 2 min, dried in a stream of nitrogen and annealed for 1 h at 180 ^oC. 1.45 M perovskite precursor solution was prepared using a 4:1 (v:v) mixed solvent from anhydrous DMF and DMSO (Sigma-Aldrich) with $FA_{0.83}Cs_{0.17}Pb(I_{0.9}Br_{0.1})_3$ composition using precursor salts: formamidinium iodide (FAI; Dyesol), cesium iodide (CsI; Alfa Aesar), PbI_2 (TCI), lead bromide ($PbBr_2$; TCI). All solutions were prepared in a nitrogen-filled glovebox and kept stirring overnight at room temperature. The perovskite precursor solution were spin-coated through a two-step spin coating program (10 s at 1000 rpm and 35 s at 6000 rpm) with dripping of anisole (Sigma-Aldrich) as anti-solvent during the second step, 10 s before the end. The films were then annealed at 100 °C for 60 min. All films were spin-coated in a drybox with relative humidity below 20%. Hole-transporting layers: (1)V1091, V1056 and V1102 solutions: we dissolved 35 mM HTMs in 1ml anhydrous chlorobenzene with additives of 14.4 µl tert-butylpyridine (tBP) and 10 µl lithium bis(trifluoromethylsulfonyl)imide (Li-TFSI) salt in acetonitrile (520 mg ml^{-1}). (2) The reference 2,20,7,70-tetrakis[*N*,*N*-di(4-methoxyphenyl)amino]-9,90-spirobifluorene (spiro-OMeTAD) solution: we dissolved 70 mM spiro-OMeTAD (Borun Technology) in 1ml anhydrous chlorobenzene with additives of 28.8 µl tert-butylpyridine (tBP) and 20 µl lithium bis(trifluoromethylsulfonyl)imide (Li-TFSI) salt in acetonitrile (520 mg ml^{-1}). After the perovskite films cooled down to room temperature, the HTM solutions were spin-coated on the perovskite layer at 2,500 r.p.m. for 40 s in a dry box (<15 RH%). We note that for stability test, we used the 35 mM host solution for both the V1091 and spiro-

OMeTAD and added the same amount of additives, which are 14.4 μl tBP and 10 μl Li-TFSI salt in acetonitrile (520 mg ml^{-1}) in 1 ml host solution.

Solar cell characterization

The *J-V* curves were measured (2400 Series SourceMeter, Keithley Instruments) under simulated AM 1.5G sunlight at 100 mW cm^{-2} irradiance generated by an Abet Class AAB sun 2000 simulator, with the intensity calibrated with an NREL calibrated KG5 filtered Si reference cell. The mismatch factor was calculated to be less than 5%, and applied to calibrate the AM 1.5 G 100 mW cm^{-2} equivalent irradiance. The active area of the solar cell measured under AM 1.5 G is 0.0919 cm^{-2}, defined by an opaque aperture mask. For the cells measured under simulated concentrated sun light, the cell area was mechanically scribed down to ~1 mm in order to reduce series resistance in the FTO. In order to determine the active area of the small cell, we measured the unmasked small cells under AM 1.5 G illumination and matched the J_{sc} measured with the same cell prior to scribing, measured through the 0.0919 cm^{-2} aperture mask. This enabled us to measure the small area cells unmasked, without inducing significant errors from estimations of small masking areas, and difficult to quantify shading losses. The forward *J–V* scans were measured from forward bias to short-circuit and the backward scans were from short-circuit to forward bias, both at a scan rate of 380 mV s^{-1}. A stabilisation time of 5 s at forward bias of 1.4 V under illumination was done prior to scanning.

The detailed synthetic procedures:

***N*,*N*-bis[2,2-bis(4-methoxyphenyl)vinyl]-4-methoxyaniline (V1056)**

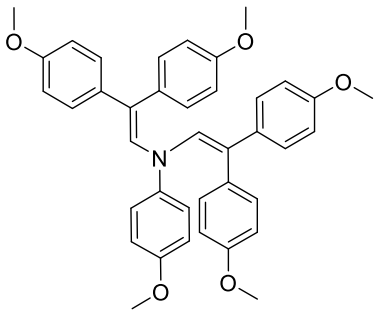

4-methoxyaniline (0.2 g, 1.6 mmol) was dissolved in toluene (4 mL + volume of the Dean-Stark trap), (+/-)camphor-10-sulphonic acid (0.37 g, 1.6 mmol) was added and the mixture

was heated at reflux for 20 minutes. Afterwards, 2,2-bis(4-methoxyphenyl)acetaldehyde (1.04 g, 4.1 mmol) was added, and reflux continued using a Dean-Stark trap. After termination of the reaction (20 min, TLC, THF:*n*-hexane, 1:4) the reaction mixture was extracted with ethyl acetate. The organic layer was dried over anhydrous Na_2SO_4, filtered and solvent evaporated. The crude product was crystallized from ethanol (15 ml). The obtained crystals were filtered off and washed with ethanol for three times. The product was recrystallized from THF/ethanol 1:2 gave as yellow crystals (0.45 g, 46%); m.p.: 190.5–192 °C.

^{1}H NMR (400 MHz, $CDCl_3$) δ: 7.06 (d, *J* = 8.9 Hz, 2H); 6.99 (d, *J* = 8.6 Hz, 4H); 6.88 (d, *J* = 8.9 Hz, 2H); 6.82 (d, *J* = 8.6 Hz, 4H); 6.63 (d, *J* = 8.7 Hz, 4H); 6.47 (d, *J* = 8.7 Hz, 4H); 5.72 (s, 2H); 3.84 (s, 6H); 3.80 (s, 3H); 3.75 (s, 6H) ppm.

^{13}C NMR (101 MHz, $CDCl_3$) δ: 159.03; 158.71; 155.20; 140.13; 134.67; 132.97; 130.74; 130.06; 128.89; 127.33; 118.24; 114.76; 113.96; 113.13; 55.87; 55.57; 55.37 ppm.

Anal. calcd for $C_{39}H_{37}NO_5$: C 78.11; H 6.22; N 2.34; found: C 78.31; H 6.12; N 2.39.

***N*,*N*,4-tris[2,2-bis(4-methoxyphenyl)vinyl]aniline (V1091)**

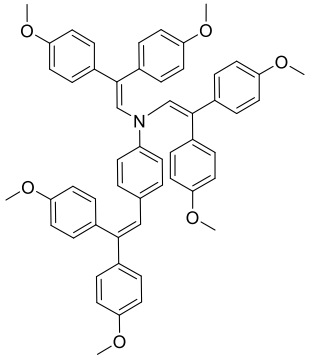

Aniline (0.2 g, 2.1 mmol) was dissolved in toluene (6 mL + volume of the Dean-Stark trap), (+/-)camphor-10-sulphonic acid (0.5 g, 2.1 mmol) was added and the mixture was heated at reflux for 20 minutes. Afterwards, 2,2-bis(4-methoxyphenyl)acetaldehyde (2.42 g, 9.45 mmol) was added, and reflux continued using a Dean-Stark trap. After termination of the reaction (6 h, TLC, THF:*n*-hexane, 1:4) the reaction mixture was extracted with ethyl acetate. The organic layer was dried over anhydrous Na_2SO_4, filtered and solvent evaporated. The crude product was purified by column chromatography using THF:*n*-hexane (v:v; 4:21) eluent. The obtained product was precipitated from acetone into 20-fold excess of methanol. The precipitate was filtered off and washed with methanol to collect **V1091** as a yellow solid (1.20 g, 69%).

^{1}H NMR (400 MHz, $CDCl_3$) δ: 7.31 – 6.78 (m, 21H); 6.61 (d, *J* = 8.5 Hz, 4H); 6.42 (d, *J* = 8.5 Hz, 4H); 5.70 (s, 2H); 3.85 (s, 6H); 3.82 (s, 3H); 3.81 (s, 3H); 3.74 (s, 6H) ppm.

^{13}C NMR (101 MHz, $CDCl_3$) δ: 159.12; 159.01; 158.83; 144.48; 139.66; 136.71; 134.41; 133.22; 132.81; 131.55; 131.27; 131.13; 130.72; 130.42; 128.96; 128.62; 126.85; 125.85; 116.28; 114.34; 113.99; 113.67; 113.13; 55.57; 55.46; 55.37; 5531 ppm.

Anal. calcd for $C_{54}H_{49}NO_6$: C 80.27; H 6.11; N 1.73; found: C 80.10; H 6.24; N 1.81.

***N*,*N*-bis[2,2-bis(4-methoxyphenyl)vinyl]aniline (V1092)**

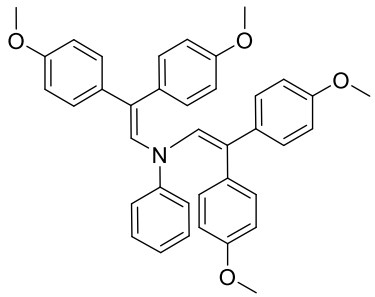

Aniline (0.1 g, 1.1 mmol) was dissolved in toluene (3 mL + volume of the Dean-Stark trap), (+/-)camphor-10-sulphonic acid (0.25 g, 1.1 mmol) was added and the mixture was heated at reflux for 20 minutes. Afterwards, 2,2-bis(4-methoxyphenyl)acetaldehyde (0.6 g, 2.3 mmol) was added, and reflux continued using a Dean-Stark trap. After termination of the reaction (2 h, TLC, THF:*n*-hexane, 1:4) the resulting precipitate was filtered off and washed repeatedly with water and then with ethanol to collect **V1092** as a yellow solid (0.4 g, 72%). The product was recrystallized from THF and dried under vacuum at 40 °C; m.p.: 249–251 °C.

^{1}H NMR (400 MHz, $CDCl_3$) δ: 7.32 (m, 2H); 7.10 (d, *J* = 7.8 Hz, 2H); 7.06 – 6.93 (m, 5H); 6.83 (d, *J* = 8.8 Hz, 4H); 6.63 (d, *J* = 8.8 Hz, 4H); 6.46 (d, *J* = 8.8 Hz, 4H); 5.77 (s, 2H); 3.85 (s, 6H); 3.75 (s, 6H) ppm.

^{13}C NMR (101 MHz, $CDCl_3$) δ: 159.14; 158.83; 146.28; 134.48; 132.88; 131.10; 130.72; 129.34; 128.97; 127.07; 121.49; 116.82; 114.01; 113.14; 55.57; 55.37 ppm.

Anal. calcd for $C_{38}H_{35}NO_4$: C 80.12; H 6.19; N 2.46; found: C 80.25; H 6.14; N 2.44.

***N*,*N*,4-tris[2,2-bis(4-methoxyphenyl)vinyl]-3,5-dimethylaniline (V1102)**

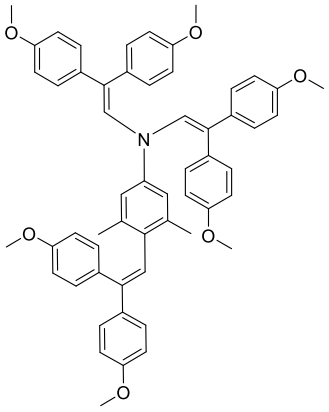

3,5-dimethylaniline (0.5 g, 4.1 mmol) was dissolved in toluene (15 mL + volume of the Dean-Stark trap), (+/-)camphor-10-sulphonic acid (1.0 g, 4.1 mmol) was added and the mixture was heated at reflux for 20 minutes. Afterwards, 2,2-bis(4-methoxyphenyl)acetaldehyde (6.3 g, 24.8 mmol) was added, and reflux continued using a Dean-Stark trap. After termination of the reaction (1 h 45 min, TLC, THF:*n*-hexane, 1:4) the reaction mixture was extracted with ethyl acetate. The organic layer was dried over anhydrous Na_2SO_4, filtered and solvent evaporated. The crude product was purified by column chromatography using THF:*n*-hexane (v:v; 4:21) eluent. The obtained product was precipitated from acetone into 10-fold excess of ethanol. The precipitate was filtered off and washed with ethanol to collect **V1102** as a yellow solid (2.0 g, 60%).

^{1}H NMR (400 MHz, DMSO-d_6) δ: 7.31-7.18 (m, 2H); 7.14- 6.48 (m, 27H); 3.85 (s, 6H); 3.82 (s, 3H); 3.94-3.51 (m, 18H); 2.26-2.10 (m, 3H); 1.59-1.32 (m, 3H) ppm.

^{13}C NMR (101 MHz, DMSO-d_6) δ: 159.26; 158.85; 158.54; 158.47; 158.08; 142.87; 135.96; 135.34; 135.06; 133.08; 131.66; 131.08; 129.51; 128.55; 127.08; 125.38; 114.43; 114.08; 114.02; 113.69; 55.59; 55.53; 55.43;55.36;55.27; 21.43; 20.46 ppm.

Anal. calcd for $C_{56}H_{53}NO_6$: C 80.45; H 6.39; N 1.68; found: C 80.10; H 6.67; N 1.81.

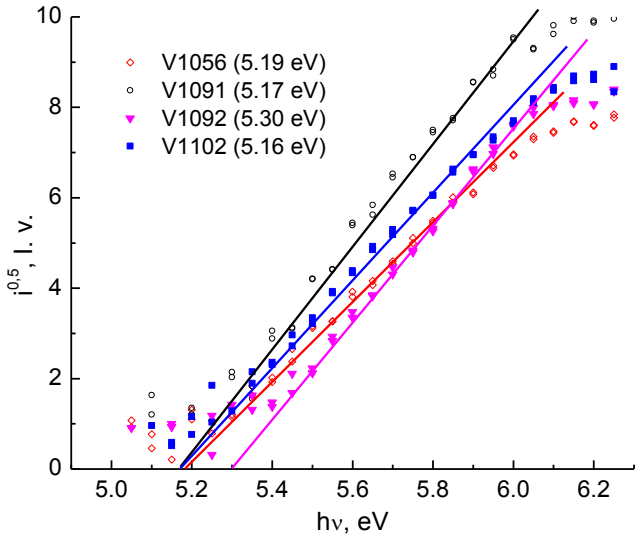

Figure S1. Photoemission in air spectra.

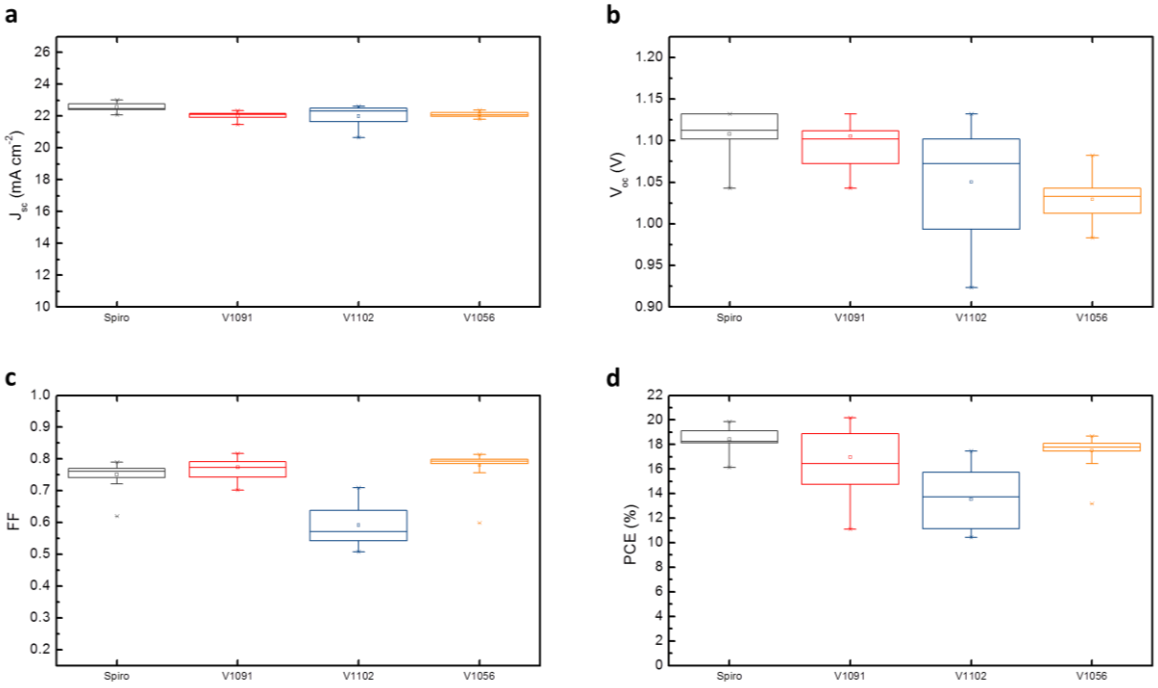

Figure S2. Statistics of J_{sc} (**a**), V_{oc} (b), FF (c) and PCE (d) of 3 batches perovskite solar cells with various hole transporting materials.

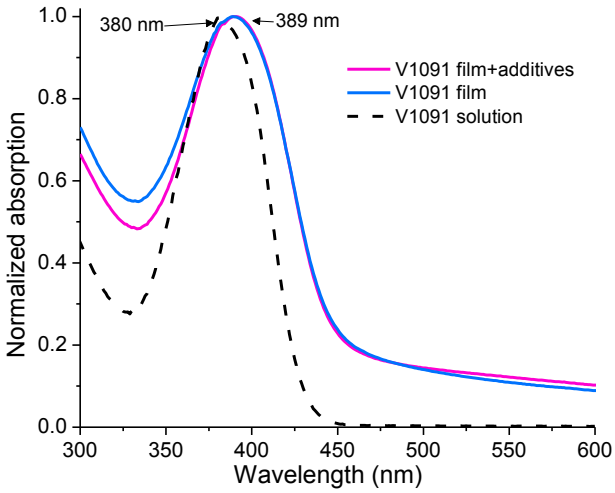

Figure S3. UV–vis absorption spectra of **V1091** from film and solution in THF (c = 10^{-4} M).

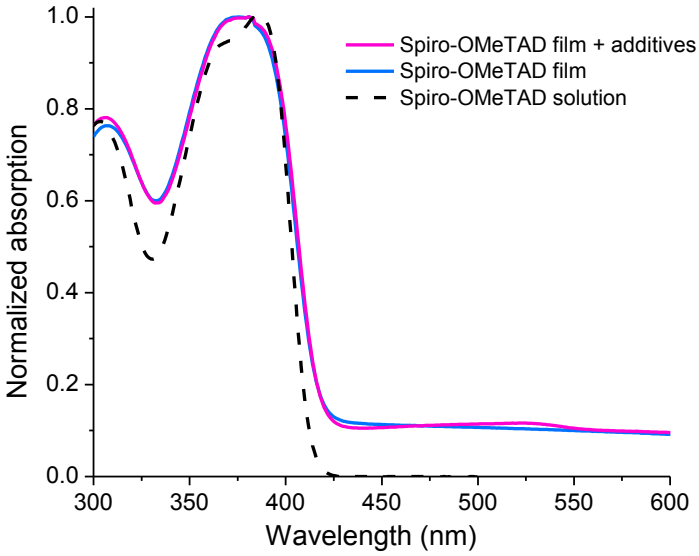

Figure S4. UV–vis absorption spectra of spiro-OMeTAD from film and solution in THF (c = 10^{-4} M).

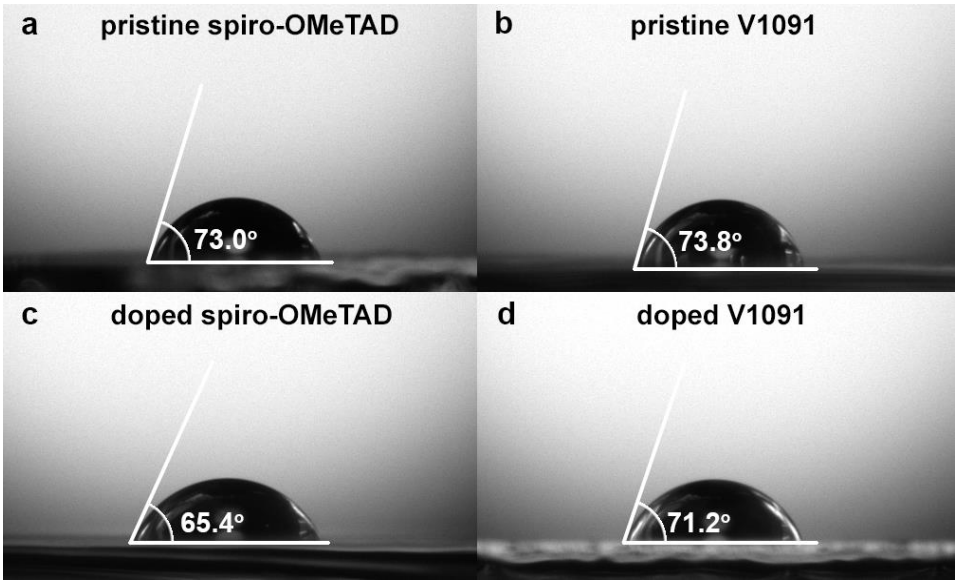

Figure S5. Contact angle measurement of the water droplet on the films of pristine spiro-OMeTAD (a); pristine V1091 (b); doped spiro-OMeTAD (c); doped V1091 (d).

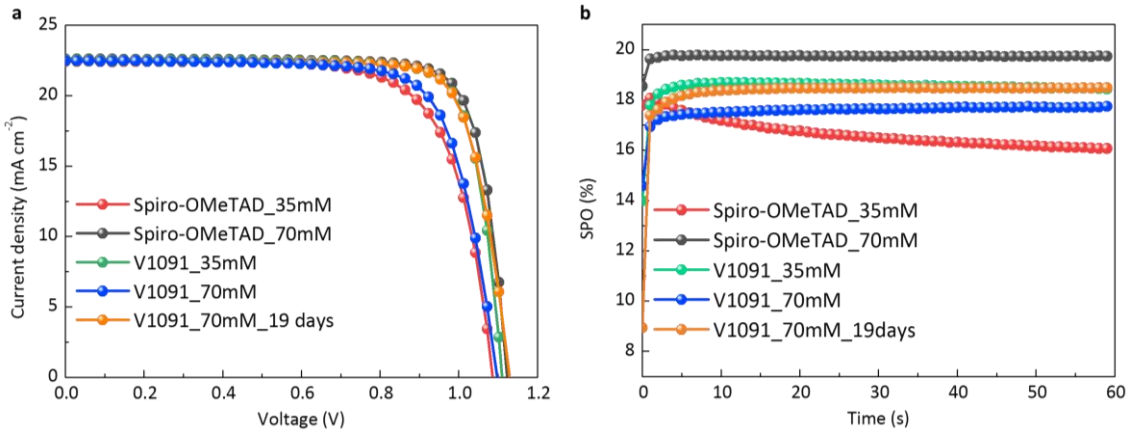

Figure S6. Effect of HTM thickness on device performance. a, J-V curves of perovskite devices with thin (35mM) and thick (70mM) layers of spiro-OMeTAD and V1091 HTMs. b, Corresponding stabilized power output. The 35 and 70 mM represent the molar concentration of HTMs in chlorobenzene. The V1091_70mM_19days sample stands for the 70mM V1091 device without encapsulation, exposed in ambient air (45 RH%) under dark condition for 19 days.

Table S1. Materials, quantities and cost for the synthesis of **V1056**.

Chemical	Weight reagent (g/g)	Weight solvent (g/g)	Weight workup (g/g)	Price of chemical (€/kg)	Cost of chemical (€/g product)	Total cost (€/g)
4-Bromoanisole	3.98			25.20	0.10	
Formic acid	20			3.87	0.08	
Sulfuric acid	4			2.63	0.01	
Methyl methoxyacetate	0.739			304	0.23	
Magnesium	0.518			104	0.06	
Diethyl ether		200		6.92	1.39	
Ethyl acetate			150	2.85	0.43	
2,2-bis(4-methoxyphenyl)acetaldehyde	29.237	200	150			2.30
2,2-bis(4-methoxyphenyl)acetaldehyde	2.323			2300	5.35	
4-Methoxyaniline	0.446			104	0.05	
10-Camphorsulfonic acid	0.842			260	0.22	
Ethanol			80	6.08	0.49	
Ethyl acetate			200	2.85	0.57	
Na_2SO_4			50	6.08	0.31	
THF			10	8.88	0.09	
Toluene		17	10	2.46	0.07	
V1056	3.611	17	350			7.15

7.15 €/g = 8.55 $/g

Table S2. Materials, quantities and cost for the synthesis of **V1091**.

Chemical	Weight reagent (g/g)	Weight solvent (g/g)	Weight workup (g/g)	Price of chemical (€/kg)	Cost of chemical (€/g product)	Total cost (€/g)
4-Bromoanisole	3.98			25.20	0.10	
Formic acid	20			3.87	0.08	
Sulfuric acid	4			2.63	0.01	
Methyl methoxyacetate	0.739			304	0.23	
Magnesium	0.518			104	0.06	
Diethyl ether		200		6.92	1.39	
Ethyl acetate			150	2.85	0.43	
2,2-bis(4-methoxyphenyl)acetaldehyde	29.237	200	150			2.30
2,2-bis(4-methoxyphenyl)acetaldehyde	2.069			2300	4.76	
Aniline	0.167			32	0.01	

10-Camphorsulfonic acid	0.417			260	0.11	
Ethanol			80	6.08	0.49	
Ethyl acetate			200	2.85	0.57	
Na_2SO_4			50	6.08	0.31	
THF			160	8.88	1.42	
Toluene		17	10	2.46	0.07	
n-Hexane			840	3.16	2.66	
Silicagel			50	64.80	3.24	
V1091	3.407	17	1390			13.64

13.64 €/g = 16.33 $/g

Supplementary References

[1] Miyamoto, E.; Yamaguchi, Y.; Yokoyama, M. *Electrophotography,* **1989**, *28*, 364.
[2] Cordona, M.; Ley, L. *Top. Appl. Phys.*, 1978, **26**, 1.
[3] Montrimas, E.; Gaidelis, V.; Pazera, A. *Lith. J. Phys*. 1966, 6, 569.
[4] Vaezi-Nejad, S. M. *Int. J. Electron.,* 1987, **62**, 361.
[5] Archie, Y.; Chan, C.; Juhasz, C. *Int. J. Electron.*, 1987, **62**, 625.
[6] Ahlrichs, R.; Bär, M.; Häser, M.; Horn, H.; Kölmel, C. *Chem. Phys. Lett.* **1989**, *162* (3), 165.
[7] Lee, C.; Yang, W.; Parr, R. G. *Phys. Rev. B* **1988**, *37* (2), 785.
[8] Becke, A. D. *J. Chem. Phys.* **1993**, *98* (7), 5648.
[9] Schäfer, A.; Horn, H.; Ahlrichs, R. *J. Chem. Phys.* **1992**, *97* (4), 2571.
[10] Weigend, F.; Ahlrichs, R.; Peterson, K. A.; Dunning, T. H.; Pitzer, R. M.; Bergner, A. *Phys. Chem.Chem. Phys.* **2005**, *7* (18), 3297.
[11] Steffen, C.; Thomas, K.; Huniar, U.; Hellweg, A.; Rubner, O.; Schroer, A. *J. Comput. Chem.* **2010**, *31* (16), 2967.